

Journal Pre-proofs

Multifunctional molecule of potassium nonafluoro-1-butanesulfonate for high-efficient perovskite solar cells

Zhaohui Wu, Jihuai Wu, Shibo Wang, Chunyan Wang, Yitiani Du, Ying Wang, Jialian Geng, Yuhe Lin, Weihai Sun, Zhang Lan

PII: S1385-8947(22)03338-1
DOI: <https://doi.org/10.1016/j.cej.2022.137851>
Reference: CEJ 137851

To appear in: *Chemical Engineering Journal*

Received Date: 8 May 2022
Revised Date: 19 June 2022
Accepted Date: 28 June 2022

Please cite this article as: Z. Wu, J. Wu, S. Wang, C. Wang, Y. Du, Y. Wang, J. Geng, Y. Lin, W. Sun, Z. Lan, Multifunctional molecule of potassium nonafluoro-1-butanesulfonate for high-efficient perovskite solar cells, *Chemical Engineering Journal* (2022), doi: <https://doi.org/10.1016/j.cej.2022.137851>

This is a PDF file of an article that has undergone enhancements after acceptance, such as the addition of a cover page and metadata, and formatting for readability, but it is not yet the definitive version of record. This version will undergo additional copyediting, typesetting and review before it is published in its final form, but we are providing this version to give early visibility of the article. Please note that, during the production process, errors may be discovered which could affect the content, and all legal disclaimers that apply to the journal pertain.

© 2022 Published by Elsevier B.V.



Multifunctional molecule of potassium nonafluoro-1-butanesulfonate for high-efficient perovskite solar cells

Zhaohui Wu, Jihuai Wu,* Shibo Wang, Chunyan Wang, Yitiani Du, Ying Wang, Jialian Geng, Yuhe Lin, Weihai Sun*, and Zhang Lan*

Engineering Research Center of Environment-Friendly Functional Materials, Ministry of Education,
Institute of Materials Physical Chemistry, Huaqiao University, Xiamen, 361021, China.

Abstract: The rapid development of perovskite solar cell (PSC) makes it a typical representative of the third generation PV technology. The large-scale manufacturing of the device still faces many challenges, such as enhancing efficiency and improving stability. The core problem is the suppression of various defects and the adjustment of energy levels among components. In this report, a multifunctional molecule of potassium nonafluoro-1-butanesulfonate (KFBS) is introduced into SnO₂ electron transport layer (ETL). Owing to the synergistic effect of potassium ion, sulfonic group and nonafluorobutane group in KFBS, the energy match between perovskite (PVK) and ETL is tuned, the PVK and ETL quality is improved, and the defects at interface, on grain boundaries and in bulk are passivated. Consequently, the power conversion efficiencies increase from 20.6% for pristine device to 23.21% for KFBS-modified device. Moreover, unpacked KFBS-modified device still maintains its initial efficiency of 90.5 % after storing at room temperature and relative humidity of 30 % in dark for 1000 h, showing an excellent environmental stability.

Keyword: perovskite solar cells; electron transport layer (ETL); tin oxide (SnO₂); potassium

* Corresponding author: E-mail address: jhwu@hqu.edu.cn; weihaisun@hqu.edu.cn; lanzhang@hqu.edu.cn

nonafluoro-1-butanesulfonate (KFBS); passivation

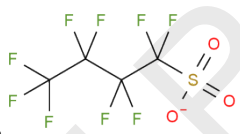
1. Introduction

Perovskite solar cells (PSCs) are regarded as the most potential inheritor of the next generation solar cells, due to the distinguished photoelectric properties of perovskite, such as long carrier lifetime, good light absorption and high defect tolerance [1-3]. Over the past few decades, the power conversion efficiency (PCE) of PSCs has raised swiftly from 3.8% to 25.7% [4,5]. TiO_2 is a frequent employed ETL in planar structure PSCs [6,7]. However, the preparation of TiO_2 is a tedious and energy-consuming process, including a sintering process at temperature higher than 400 °C [8-10], which hinders the large-scale processing of PSCs. In addition, TiO_2 can photocatalytic degrade perovskite, which damages the stability of the device (especially under ultraviolet light) [11-13]. In this sense, SnO_2 is a competitive substitute for TiO_2 since it has higher electron mobility, better optical stability and more suitable band alignment compared to TiO_2 [14-16]. Recently, Min et al. inserted a coherent interlayer between SnO_2 ETL and perovskite layers, realized by coupling Cl-bonded SnO_2 with a Cl-containing perovskite precursor, leading to a certified PCE of 25.5%, which is the best efficiency in published SnO_2 -based PSCs [17].

Although SnO_2 has some outstanding properties, it still has some shortages to be improved. Oxygen vacancies and uncoordinated Sn^{4+} defects are inevitable during the preparation of SnO_2 by solution method [18-20]. These defects will seriously hinder the transportation of charge carriers, enabling charge accumulation at the interface of ETL/perovskite (PVK) and triggering non-radiative recombination [21,22]. In addition, the energy level matching among ETL and PVK is also a key factor affecting carrier transportation of the device [23,24]. Xing et al. demonstrated the passivation of defects by using an organic molecular carbon-halogen band (C-X) with strong electronegativity [25]. Dong et al. investigated the interaction between chlorobenzenesulfonic salts and uncoordinated Sn to compensate for the defects on the surface

of SnO₂ film [26]. Zhang et al. proposed zwitterion 3-aminopropanesulfonic acid (APS) as an additive, in which the sulfonic acid group passivates both deep and shallow energy level defects, and suppresses ion migration and non-radiative recombination in perovskite films [27]. Zhu et al. proposed that the efficiency of PSCs was significantly improved by adding KCl into the SnO₂ ETL, and the defects at the SnO₂/PVK interface and grain boundaries of PVK film were passivated [28]. Jung et al. found that NH₄F could adjust the Fermi level of SnO₂ and build a greater energy level gradient with perovskite layer. [29]. Park et al. modified SnO₂ ETL by zwitterionic compound 3-(1-pyridinio)-1-propanesulfonate, to make the SnO₂ work function shift, so as to promote more convenient charge transfer [30].

Most of the above researches only focused on defect passivation or energy level adjustment, while the defect passivation often only concerned on the surface or interface. In this work, we introduced a multifunctional surfactant of potassium nonafluoro-1-

butanesulfonate (KFBS,  [31]) into the SnO₂ ETLs. The nonafluorocarbon alkyl chains of KFBS molecule bond with under-coordinated Sn²⁺ ions in SnO₂, which effectively inhibits the charge recombination caused by defects related to oxygen vacancies; the potassium ion (K⁺) could ameliorate the crystal quality and increase the size of grains of perovskite, adjust the energy level matching between SnO₂ and perovskite; the sulfonate group could interact with uncoordinated Pb²⁺ ions to reduce the surface defects and suppress carrier non-radiative recombination. In a word, the performance and stability of PSCs could be improved due to the multiple synergistic effect of the above special ions and groups in KFBS molecule. As a consequence, the power conversion efficiencies increase from 20.6% for pristine device to 23.21% for KFBS-modified device.

2. Result and discussion

The KFBS was introduced into SnO_2 precursor solution and spin-coated on ITO for forming an KFBS-modified electron transport layer (ETL). The top-view scanning electron microscopy (SEM) was applied to observe the morphology of the pristine and KFBS-modified SnO_2 films (Figure S1a, b, in Supplementary Materials). The pristine SnO_2 has partial agglomeration, while the agglomeration is significantly improved after the addition of KFBS.

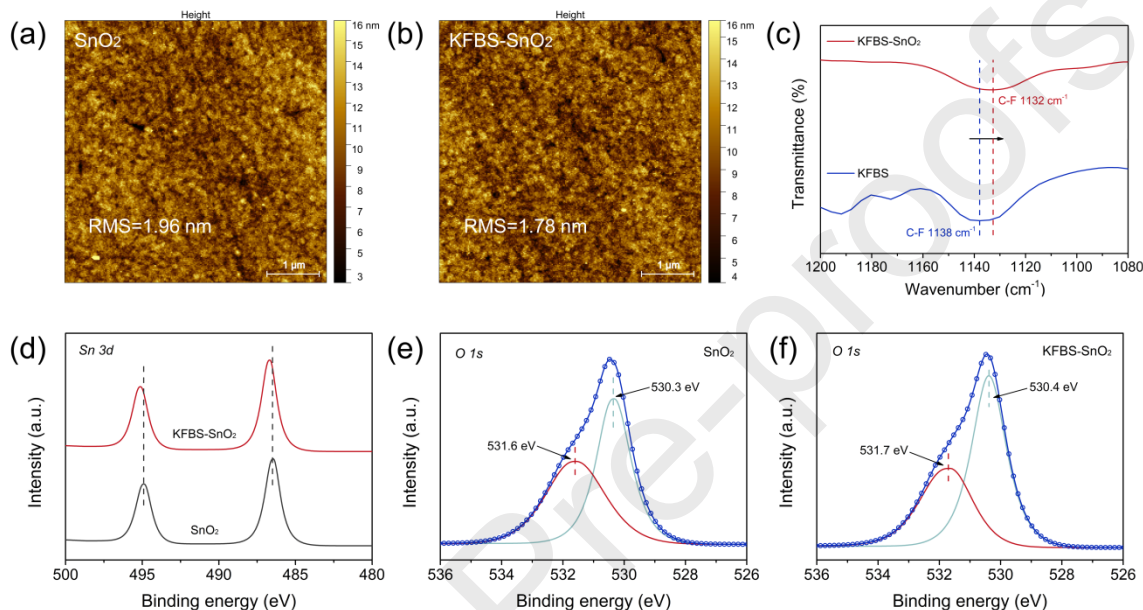


Fig. 1. Atomic force microscopy (AFM) images of (a) SnO_2 and (b) KFBS- SnO_2 . (c) FTIR spectra of KFBS and KFBS- SnO_2 . XPS spectra of (d) SnO_2 and KFBS- SnO_2 in Sn 3d region. (e) SnO_2 in O 1s region and (f) KFBS- SnO_2 in O 1s region.

The roughness of SnO_2 and KFBS- SnO_2 ETL was monitored by atomic force microscopy (AFM). The root mean square (RMS) of the two films surface are 1.96 nm and 1.78 nm, respectively (Fig. 1a, b), which are consistent with the results observed by SEM. This might be due to the fact that KFBS is a surfactant that effectively prevents the agglomeration of SnO_2 nanocrystals [32]. The Zeta potential measurement was carried out to characterize the size of SnO_2 particles. The Zeta potential of KFBS- SnO_2 was -26.08 mV, which was lower than that of the pristine SnO_2 (-13.22 mV). The higher absolute value of the Zeta potential indicates a smaller dispersed particle size and a more stable system after the addition of KFBS, which means less particle aggregation of SnO_2 by KFBS [33].

The fourier transform infrared (FTIR) spectra of KFBS and KFBS-SnO₂ were studied and shown in Fig. 1c. For KFBS sample, the stretching vibration peak at 1138 cm⁻¹ corresponds to the C–F band; For KFBS-SnO₂ sample, the peak is shifted to 1132 cm⁻¹. However, the characteristic peak of S=O did not shift significantly (Figure S2), which implies the interaction between F and Sn may occur. Fig. 1d exhibits the X-ray photoelectron spectra (XPS) of SnO₂ and KFBS-SnO₂ in Sn 3d region, two main peaks located at 486.49 and 494.91 eV correspond to Sn 3d_{5/2} and Sn 3d_{3/2} states of Sn⁴⁺, respectively. After doping, all Sn 3d peaks shift to higher binding energies, attributable to the alteration of the chemical environment for Sn⁴⁺, indicating a strong interaction between Sn and KFBS [34]. This may be explained by the formation of coordination bonds between the empty orbital of Sn in tin oxide and the high-electronegative F in KFBS [25]. The change in the binding energy of O 1s further corroborates the results described above. In the XPS of the O 1s region for SnO₂ shown in Fig. 1e, two main peaks at 530.3 eV and 531.6 eV should come from the lattice oxygen (denoted O_{la}) and oxygen vacancy (denoted O_{va}) in SnO₂ film, respectively [35]. The ratio of O_{la} to O_{va} increased from 1.09 to 1.53 after the addition of KFBS to SnO₂ (Fig. 1f, and Table S1 lists the main parameters of O 1s peak in SnO₂ and KFBS-SnO₂), which indicated that the oxygen vacancies in SnO₂ films are effectively restrained [36]. Since oxygen vacancies in SnO₂ usually become traps for photogenerated carriers, the reduction of oxygen vacancies leads to a reduction in the loss of photogenerated carriers during transportation.

Two-step method was used to deposit PVK on ETL. In the first step, the PbI₂ solution was spin-coated on the ETL. Observing the top-view SEM images as illustrated in Figure S3, the PbI₂ layer, which was spin-coated on KFBS-modified SnO₂, has larger grains, bigger pores and more uniform particle size distribution than that on pristine SnO₂. Larger grains and uniform size distribution mean less nucleation sites, which contribute to enhance the crystal quality of perovskite by a slow and uniform crystal growth on KFBS-modified SnO₂ [37]. The

more and bigger pores in PbI_2 allow the solution to diffuse fully into the film to react adequately with PbI_2 when the organic amine solution was spin-coated, resulting in the denser and larger perovskite grains.

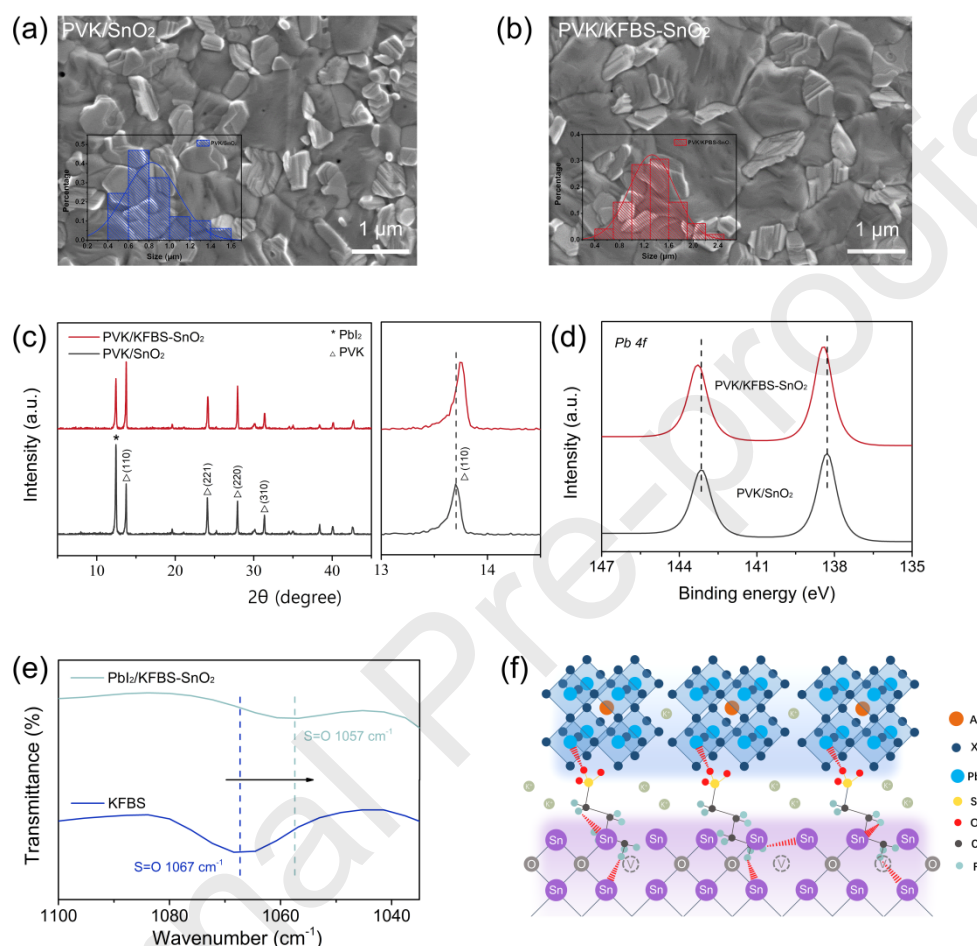


Fig. 2 Top-view SEM images of (a) PVK/SnO₂ and (b) PVK/KFBS-SnO₂ films (the inset: the size distribution of the grains). XRD patterns of (c) PVK/SnO₂ and PVK/KFBS-SnO₂ films, the right is the enlargement in 13°~14.5°. (d) XPS spectra of PVK/SnO₂ and PVK/KFBS-SnO₂ films in Pb 4f region. (e) FTIR spectra of KFBS and PbI₂/KFBS-SnO₂. (f) The possible interaction mechanism among KFBS, SnO₂ and perovskite.

After PbI_2 depositing on the ETL, mixed organic amine solution was spin-coated the PbI_2 /ETL films to form perovskite layer on it. The morphologies of PVK/SnO₂ and PVK/KFBS-SnO₂ films are observed with top-view SEM images. As seen in Fig. 2a, b, there

are many pinholes in the PVK/SnO₂ films, which provide active sites for carrier recombination and lead to voltage loss. However, the quality of PVK/KFBS-SnO₂ film has been greatly improved, accompanied by the disappearance of pinhole defects and the concentrated distribution of PbI₂ at the grain boundaries. From the inset, it can know that the average grain size of PVK increase from 0.83 μm for the PVK/SnO₂ film to 1.31 μm for the PVK/KFBS-SnO₂ film (Figure S4). The quality improvement of PVK/KFBS-SnO₂ film is further verified by the AFM images displayed in Figure S5. The RMS of surface roughness is reduced from 44.2 nm for the PVK/SnO₂ film to 32.3 nm for the PVK/KFBS-SnO₂ film. In additions, we observed the cross-view SEM image of KFBS-modified PSC shown in Figure S6, it can be seen that the high quality and the thickness of 800 nm PVK is grown on the high-quality KFBS-SnO₂ ETL. The modification of KFBS not only improves the quality of ETL, but also ameliorate the quality of PVK grown on ETL, which lays a good foundation for the device to boosts photovoltaic performance of devices.

X-ray diffraction (XRD) patterns of PVK/SnO₂ and PVK/KFBS-SnO₂ films are shown in Fig. 2c. No new peak appears after addition of KFBS, indicating that KFBS do not have any influence on the crystal structure of perovskite. However, the PVK/KFBS-SnO₂ film has strong diffraction peaks intensity for the (110) lattice plane, which demonstrates that a valid improvement in the crystallinity of the perovskite is indeed achieved. Further comparative analysis shows that the (110) lattice plane of the perovskite film has shifted from 13.70° for the PVK/SnO₂ film to 13.75° for the PVK/KFBS-SnO₂ film (the right in Fig. 2c). The shift of the peak position to a higher angle is related to the reduction of d-spacing and lattice distortion (d-spacing decrease from 0.6456 nm for the PVK/SnO₂ film to 0.6433 nm for the PVK/KFBS-SnO₂ film), which may be attributed to the participation of potassium ions (K⁺) in KFBS in the formation of perovskite crystals by migration from the ETL into the perovskite layer [38, 39]. This will delay the crystallization of the as-cast precursor film to a certain extent, thereby

extending the processing window [40]. Figure S7 presents a comparison photograph of PVK/SnO₂ and PVK/KFBS-SnO₂ films annealed at 30 °C for 120 s. It can be distinctly observed that the perovskite films based on the pristine SnO₂ exhibit a darker color at 0 s and a shorter process of forming the black phase compared to the PVK/KFBS-SnO₂ films. The photographs further provide the evidence that the introduction of K⁺ ion delayed the transformation process, which is beneficial to the transformation of perovskite (Fig. 2c) and the improvement of crystal quality (Fig. 2b). Also, it's worth noting that appropriate PbI₂ is beneficial to improve the performance of PSCs in the perovskite prepared by two-steps [41-43].

XPS spectra of perovskite films [44, 45] in the binding energy at Pb 4f region is shown in Fig. 2d. For the pristine perovskite film, Pb 4f_{7/2} and Pb 4f_{5/2} transitions are 138.28 eV and 143.16 eV, respectively, as for KFBS-modified perovskite film, Pb 4f_{7/2} and Pb 4f_{5/2} transitions move to 138.43 eV and 143.30 eV, respectively, indicating an interaction between Pb and KFBS. To understand the interaction, FTIR spectra of KFBS and PbI₂/KFBS-SnO₂ films were characterized and exhibited in Fig. 2e (full spectrum in Figure S2). The stretching vibration peak of the S=O bond in the KFBS feedstock is located at 1067 cm⁻¹, while in PbI₂/KFBS-SnO₂ this peak position is shifted to 1057 cm⁻¹. The shift may be caused by the interaction between the sulfonic group (–SO₃[–]) on KFBS and the Pb, we set up a KFBS-SnO₂ control group and found that the S=O peak did not exhibit a noticeable displacement. Therefore, it can be concluded that uncoordinated Pb can coordinate with S=O, lowering the S=O electron cloud density [46, 47], which may be a critical reason for the remarkable improvement of phase stability to perovskite after the addition of KFBS in the ETL.

On the basis of aforementioned discussions, a possible interaction mechanism among KFBS, SnO₂ and perovskite is presented in Fig. 2f. O atom and F atom with high electronegativity and lone electron pair, on sulfonic group and on nonafluorobutane group in

KFBS, interact with uncoordinated Sn in ETL and uncoordinated Pb in PVK, thereby passivate the defects on grain boundaries, at the interface and in bulk of ETL and PVK, suppress carrier non-radiative recombination and boost the photovoltaic performance of the device. Meanwhile, the crystal quality of perovskite films is optimized by diffusion of potassium into perovskite.

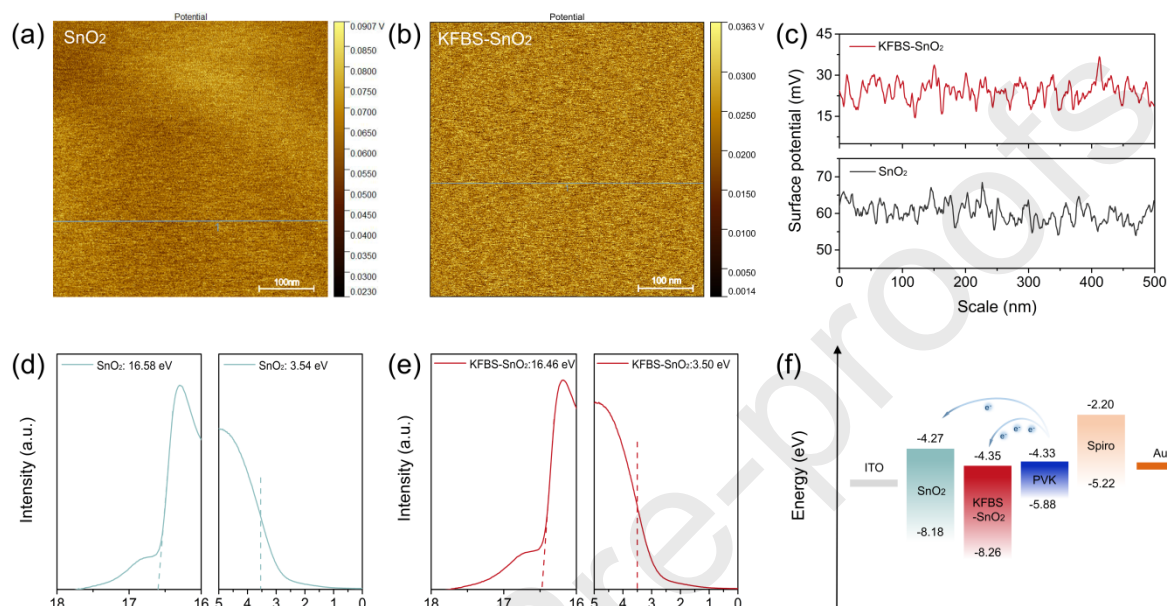


Fig. 3 Kelvin probe force microscopy (KPFM) image of (a) SnO₂ film and (b) KFBS-SnO₂ film. (c) Surface potential of SnO₂ and KFBS-SnO₂ from KPFM images, respectively. (d) UPS spectra of SnO₂ film in the region of E_{onset} (left) and E_{cutoff} (right) binding energy. (e) UPS spectra of KFBS-SnO₂ film in the region of E_{onset} (left) and E_{cutoff} (right) binding energy (f) Energy level diagram of perovskite solar cells.

To investigate the surface potential distribution of the SnO₂ films with and without the addition of KFBS, Kelvin probe force microscopy (KPFM) was implemented, as displayed in Fig. 3a, b. Based on the KPFM images, the surface potential of KFBS-SnO₂ films and SnO₂ films can be obtained (Fig. 3c). As it can be noticed, the KFBS-SnO₂ film has more uniform surface energy distribution and lower average surface potential of 24.1 mV than SnO₂ film (60.2 mV).

The optical transmission spectra of SnO₂ and KFBS-SnO₂ films were recorded and revealed in Figure S8a. Based on the spectra, the Tauc plot of SnO₂ and KFBS-SnO₂ films is

drawn in Figure S8b. Apparently, the incorporation of KFBS made no significant effect on the transmittance of SnO₂ film in the visible region (Figure S8a). The optical band gap (E_g) of SnO₂ and KFBS-SnO₂ ETL is the same from Tauc plot (Figure S8b), both showing a E_g value of about 3.91 eV.

Figure S9 shows the ultraviolet photoelectron spectroscopy (UPS) full spectra of SnO₂ and KFBS-SnO₂ films. According to the full UPS spectra, the E_{onset} and E_{cutoff} of SnO₂ film and KFBS-SnO₂ film can be determined and shown in Fig. 3d and 3e, respectively. The Fermi levels (E_F) is acquired from the difference value between the photon energy of irradiation light ($h\nu = 21.22$ eV) and the cut-off binding energy of electron: $E_F = h\nu - E_{\text{cutoff}}$. The maximum valence band (E_{VB}) is obtained from the formula: $E_{\text{VB}} = -E_F - E_{\text{onset}}$, and the minimum conduction band (E_{CB}) is obtained from the formula: $E_{\text{CB}} = E_{\text{VB}} + E_g$ [8, 48]. The calculation results are shown in Table S2 and Fig. 3f. As can be seen, the E_{CB} values of SnO₂ and KFBS-SnO₂ can be calculated as -4.27 eV, and -4.35 eV, respectively. While the E_{CB} values of PVK is -4.33 eV. Obviously, the lower E_{CB} value of KFBS-SnO₂ ETL (-4.35 eV) than PVK (-4.33 eV) makes the effective electrons extraction and transportation from PVK to ETL. On the contrary, the higher E_{CB} value of pristine SnO₂ ETL (-4.27 eV) than PVK (-4.33 eV) hinders the electrons effective transportation and easily cause the accumulation of carriers at the interface of ETL/PVK and energy loss. The introduction of KFBS into SnO₂ constructs a smooth energy gradient, which is favorable for carrier extraction and voltage enhancement [49].

Steady-state photoluminescence (PL) and time-resolved photoluminescence (TRPL) characterizations were applied to analyze the carrier transportation dynamics of PSCs. From Fig. 4a, it is evident that the PL intensity of the KFBS-SnO₂/PVK is weaker than that of SnO₂/PVK, which is due to the improvement of electron transportation and extraction ability by KFBS addition. TRPL profile of ITO/PVK, SnO₂/PVK and KFBS-SnO₂/PVK films are presented in Fig. 4b, the TRPL profiles are fitted with an exponential function [50]: $I(t) =$

$A_1 \exp(-t/\tau_1) + A_2 \exp(-t/\tau_2) + B$. Where A_1 and A_2 represents the decay amplitudes; B is a constant; τ_1 is related to the fast decay of non-radiative recombination associated with the defects and τ_2 refers to the slow decay of radiative recombination. The PL average life (τ_{ave}) is calculated by the formula [8, 51]: $\tau_{ave} = \sum \frac{A_i \tau_i^2}{A_i \tau_i}$. From the results shown in Table S3, the modification of KFBS speeds up the PL decay with a quicker PL decay rate (τ_{ave} : 58.94 ns) than that of the pristine film (τ_{ave} : 90.10 ns), authenticating the trap-assisted recombination is mitigated partly [8].

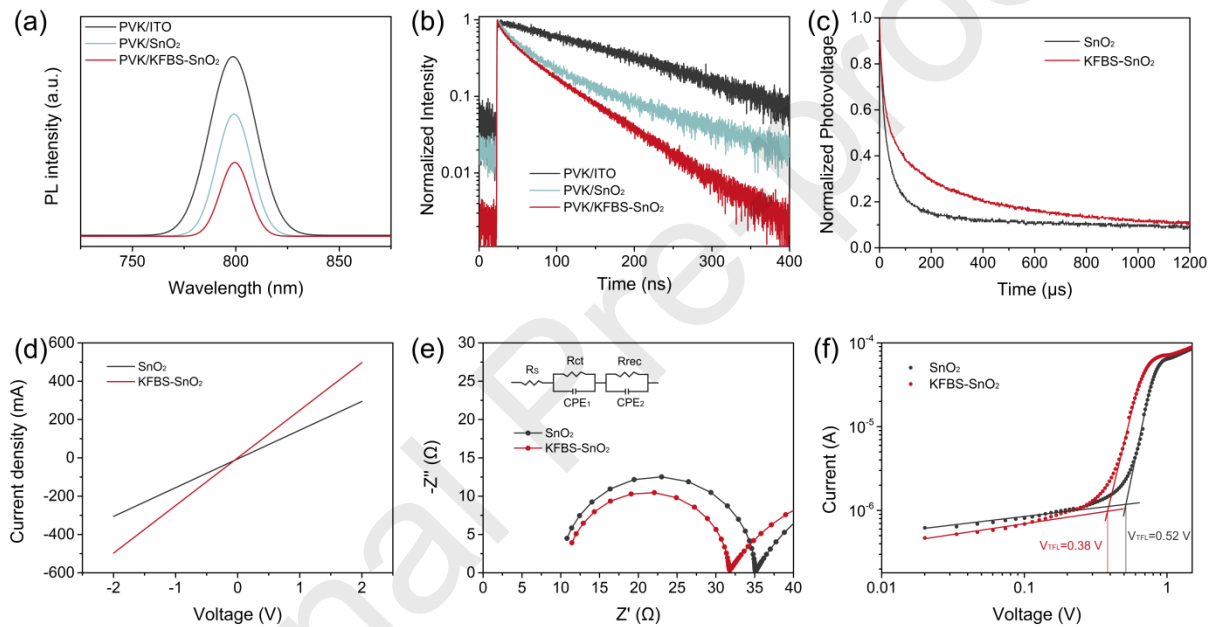


Fig. 4 (a) Steady-state photoluminescence (PL) and (b) Time-resolved photoluminescence (TRPL) spectra of PVK on ITO, SnO₂ and KFBS-SnO₂. (c) The transient photovoltage (TPV) curves of PSCs based on SnO₂ and KFBS-SnO₂ measured in dark. (d) Dark J - V characteristics of the devices with ITO/SnO₂ (or KFBS-SnO₂)/Ag. (e) Nyquist plots of PSCs based on SnO₂ and KFBS-SnO₂. (Inset: equivalent circuit). (f) SCLC characteristics of electron-only devices based on SnO₂ and KFBS-SnO₂.

Transient photovoltage (TPV) decay curves of the SnO₂ and KFBS-SnO₂ devices are exhibited in Fig. 4c. Charge carrier recombination time (τ_r) of KFBS-SnO₂ device (182.7 μs) significantly extended than the SnO₂ device (53.0 μs) via TPV analysis. The slower carrier

recombination rate is attributed to the improvement of energy level gradient between PVK and ETL and the reduction of trap-assisted recombination by KFBS treatment [52].

We measured the J - V curves under the dark conditions for the device with ITO/SnO₂ (or KFBS-SnO₂)/Ag structure, as presented in Fig. 4d, the conductivity (σ_0) of SnO₂ and KFBS-SnO₂ films can be calculated based on the formula [53]: $\sigma_0 = Id/AV$, where d is the thickness of ETL obtained from the device's cross-view SEM image, shown in Figure S6; A is the effective area of the device about 0.09 cm². The results show that the conductivity (σ_0) increases from $5.00 \times 10^{-6} \text{ S} \cdot \text{cm}^{-1}$ for the pristine SnO₂ to $8.29 \times 10^{-6} \text{ S} \cdot \text{cm}^{-1}$ for the KFBS-SnO₂ film, which is possibly due to the addition of carrier concentration caused by the introduction of K⁺ ion from KFBS.

Electrochemical impedance spectroscopy (EIS) was employed to elucidate the charge carrier recombination and transportation in the device. Fig. 4e shows the fitted Nyquist diagram, and the inset is the equivalent circuit for fitting, fitted results are displayed in Table S4. The curves contain two arcs, in which the charge transfer resistance (R_{ct}) is located in the arc of the high-frequency region, and the other charge recombination resistance (R_{rec}) is located in the arc of the low-frequency region. [54]. The KFBS-modified device has a smaller R_{ct} (20.97 Ω) and a larger R_{rec} (39.66 Ω) than the pristine device (R_{ct} : 45.65 Ω , R_{rec} : 25.06 Ω), indicating that the KFBS-modified device has an easier carrier transfer at the PVK/ETL interface and a more difficult carrier non-radiative recombination [55].

To quantitatively appraise the trap density, we measured space charge limited current (SCLC) of the devices that have a structure of ITO/SnO₂ (or KFBS-SnO₂)/PVK/PCBM/Ag. From the turning point of the curve slope in Fig. 4f, the trap-filled limit voltage (V_{TFL}) for the devices utilizing SnO₂ and KFBS-SnO₂ as substrates are 0.52 V and 0.38 V, respectively. Therefore, trap-state density (N_t) is computed based on the formula [56]: $N_t = 2\epsilon\epsilon_0 V_{TFL}/qL^2$. the trap-state density (N_t) decreases from $2.59 \times 10^{15} \text{ cm}^{-3}$ for pristine device to $1.89 \times 10^{15} \text{ cm}^{-3}$

KFBS-modified device, which is quantitative evidence of defect passivation by KFBS additions [57].

The built-in potential (V_{bi}) of the device can be obtained from the Mott-Schottky curves acquired by capacitance-voltage (C-V) measurement, that is presented in Figure S10. and the V_{bi} of the device reaches 1.05 V after the introduction of KFBS in the SnO_2 layer, which is larger than the V_{bi} value of 0.95 V for the pristine device. The larger built-in potential can establish a more robust driving force for the detachment of carriers at the interface and reduce the recombination caused by the charge accumulation at the interface [58].

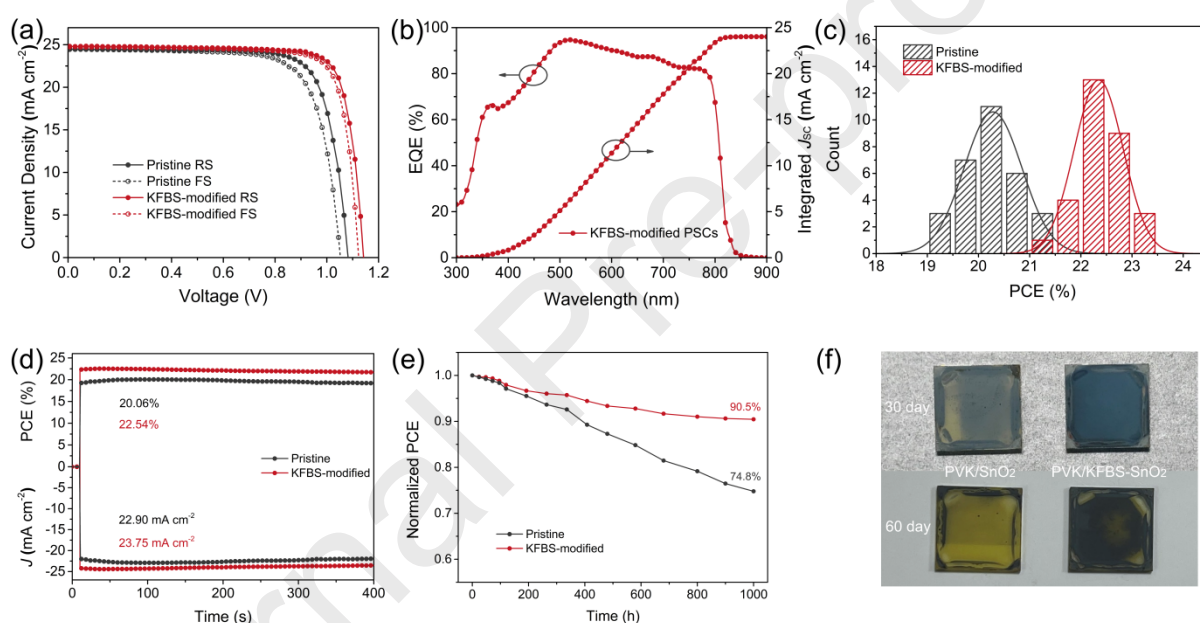


Fig. 5 (a) $J-V$ curves of pristine and KFBS-modified PSCs by forward and reverse scans. (b) EQE and integrated J_{sc} of the KFBS-modified device. (c) Statistics histogram of PCEs of the pristine and KFBS-modified PSCs (a batch of 30 cells). (d) Steady-state PCE and J_{sc} output of the pristine and KFBS-modified PSCs. (e) Environmental stability of unencapsulated devices stored at room temperature and relative humidity of 30%. (f) Photographs of PVK/ SnO_2 and PVK/KFBS- SnO_2 film after storing for 30 and 60 days at room temperature and relative humidity of 30%.

The planar PSC with the structure of ITO/ SnO_2 (or KFBS- SnO_2)/PVK/spiro-OMeTAD/Ag was fabricated, and the cross-view SEM image of KFBS-modified PSC is

displayed in Figure S6. To optimize the KFBS concentration condition, the comparative experiment of the PSC modified with different KFBS concentrations was carried out, the result is shown in Figure S11. As a consequence, the optimal KFBS concentration in this n-i-p planar structure PSCs is determined as $0.3 \text{ mg}\cdot\text{mL}^{-1}$. Under this optimized condition, the PSC realized a highest PCE of 23.21%, along with $V_{\text{OC}} = 1.144 \text{ V}$, $J_{\text{SC}} = 24.83 \text{ mA}\cdot\text{cm}^{-2}$, $\text{FF} = 81.71\%$, which is dramatically higher than that of the pristine device ($\text{PCE} = 20.60\%$, $V_{\text{OC}} = 1.082 \text{ V}$, $J_{\text{SC}} = 24.47 \text{ mA}\cdot\text{cm}^{-2}$, $\text{FF} = 77.81\%$). The main reason is the improvement of PVK and ETL quality, the alignment of energy level gradient between PVK and ETL, and the reduction of trap-state density at interface, on grain boundaries, and in bulk by KFBS addition.

Perovskite solar cells have an unavoidable hysteresis effect. The hysteresis of the device can be studied by comparing the J - V curves obtained from forward (FS) and reverse (RS) scanning. According to definition hysteresis index ($\text{HI} = (\text{PCE}_{\text{RS}} - \text{PCE}_{\text{FS}}) / \text{PCE}_{\text{RS}}$) [59]. Fig. 5a shows the J - V curves for the FS and RS scanning of the pristine and KFBS-modified PSCs, the parameters are recorded in Table S5. The HI of the pristine and KFBS-modified devices are 0.065 and 0.028, respectively. The smaller hysteresis behavior for the KFBS-modified devices than the pristine is thanks to the adjustment of potential barrier and the alleviation of carrier accumulation at the interface of PVK/ETL caused by KFBS treatment. Fig. 5b shows the external quantum efficiency (EQE) and integrated J_{SC} of the KFBS-modified device. The device obtains an integrated J_{SC} of $24.02 \text{ mA}\cdot\text{cm}^{-2}$, which is well consistent with the J_{SC} average value acquired from the J - V curves ($24.83 \text{ mA}\cdot\text{cm}^{-2}$), verifying the reliability of J - V and other photovoltaic data measurement (the EQE and integrated J_{SC} of the pristine device was $23.58 \text{ mA}\cdot\text{cm}^{-2}$, displayed in Figure S12).

The repeatability of the device was assessed by measuring the PCE of a batch of 30 devices. According to the efficiency distribution in Fig. 5c, the average PCE for the device using the KFBS-SnO₂ ETL is 22.8%, which is better than that of the pristine device (20.6%).

Moreover, the modified device has more concentrated efficiencies distribution, indicating a better repeatability than the pristine device. Figure S13 shows box diagrams of V_{OC} , J_{SC} , PCE, and FF based on statistic measurements of the pristine and KFBS-modified PSCs (relevant statistical data are exhibited in Table S6). The results are identical with the Fig. 5c.

The device stability is also a critical issue, the steady-state PCE and J_{SC} output of the pristine and KFBS-modified PSCs are shown in Fig. 5d. A bias voltage of 0.875 and 0.948 V was exerted on the PSCs based on SnO_2 and KFBS- SnO_2 ETLs, and eventually the stabilized PCE of them got 20.06% and 22.54%, respectively, over continuous AM 1.5 G illumination, demonstrating an excellent operation stability.

The environmental stability was evaluated by storing unencapsulated devices at room temperature and relative humidity of 30% in dark for 1000 h. From Fig. 5e, KFBS-modified device still maintains the initial efficiency of 90.5 %, while the pristine device only left 74.8 % of the initial efficiency, demonstrating an excellent environment stability of the modified device. Simultaneously, we observed and recorded the appearance change of the PVK/ SnO_2 and PVK/KFBS- SnO_2 film after 30 and 60 days under the same storing conditions. As can be observed from Fig. 5f, the perovskite in PVK/KFBS- SnO_2 film can stably existed in black phase, while the perovskite in PVK/ SnO_2 film is transformed into yellow phase. The main reason is that the introduction of KFBS successfully passivates the perovskite grain boundaries and the defects in bulk, thereby stabilizing the perovskite phase.

3. Conclusions

In summary, this work demonstrated a simpleton and efficient tactics to improve the performance of PSCs by implanting a multifunctional surfactant (KFBS) as an additive into SnO_2 ETL. The accession of KFBS optimizes the energy level matching between SnO_2 and PVK, and effectively passivates the defect at interface, on grain boundaries and in bulk, with

the consequence of enhancing the carrier extraction and inhibiting the charge carrier recombination. Meanwhile, the modification of KFBS improves the quality of SnO₂ and PVK, and enhance the stability of devices. Owing to the multifunction of KFBS, the KFBS-modified (0.3 mg·mL⁻¹) PSC achieves a champion PCE of 23.21%, in comparison to the efficiency of 20.60% obtained by the pristine device under the identical conditions. In addition, unpacked KFBS-modified device still maintains its initial efficiency of 90.5 % after storing at RT and RH 30% in dark for 1000 h, showing an excellent environmental stability.

4. Experimental section

4.1. Materials

For all chemicals, they are utilized directly in equipment preparation without purification. Isopropanol (IPA, 99.5%), N, N-dimethylformamide (DMF, > 99.9%), dimethyl sulfoxide (DMSO, > 99.9%) and chlorobenzene (CB, 99%) were bought from Sigma-Aldrich. Indium tin oxide (ITO, 14 Ω sq⁻¹), lead iodide (PbI₂, 99.99%) and methylammonium iodide (MAI, ≥ 99.5%) were purchased from Advanced Electronic Technology Co., Ltd. methylamine hydrochloride (MAH, 99.5%) and formamidinium iodide (FAI) were acquired from Xi'an Bright Optoelectronics Technology Co., Ltd. SnO₂ aqueous colloidal precursor (tin(IV) oxide) was obtained from Alfa Aesar. Spiro-OMeTAD was purchased from Shenzhen Fermi Science and Technology Company. Bis(trifluoromethane) sulfonimide lithium salt (Li-TFSI, 99.95%), 4-tert-butylpyridine (tBP, 98%) and acetonitrile (99.8%) were acquired from Sigma-Aldrich. Potassium nonafluoro-1-butanesulfonate (KFBS, 97%) was obtained from Aladdin

4.2. Device fabrication

Perovskite solar cells were fabricated with ITO/SnO₂ (or KFBS-SnO₂)/perovskite/spiro-OMeTAD/Ag as construction. Indium tin oxide (ITO) substrate was cleaned with detergent, acetone and ethanol in ultrasonic bath for 30 min. Then the cleaned and dried substrates were

put into the ultraviolet ozone cleaner for 20 min. Dissolve quantitative potassium nonafluorooctanesulfonate (KFBS) in deionized water at concentration, stir for 10 min and then mix the solution with commercial SnO_2 precursor solution at 1:4. The mixed solution has been spin-coated on ITO at 3500 rpm for 25 s, and then annealed at 180 °C for 30 min to obtain the corresponding ETL, which was conducted in air. After cooling, the SnO_2 films need to be treated in UV ozone for 15 min before the next step. A two-step method was adopted to prepare the perovskite layer in the N_2 glove box. At first, 0.6915 g PbI_2 was solubilized in 900 μL DMF and 100 μL DMSO solution, and then the PbI_2 solution was applied to the ETL-coated substrate by spin-coated (1500 rpm for 30 s), followed by annealing at 70 °C for 1 min. Then MAI, MACl, FAI (MAI/MACl/FAI = 0.00639: 0.0090: 0.0900 g) were solubilized in 1mL IPA to form an organic amine solution, spin-coated on PbI_2 coated substrate (2000 rpm for 30s), followed by pre-annealed at 30 °C for 5min and then annealed at 150 °C for 15 min. Formation of perovskite layers with $\text{FA}_{1-x}\text{MA}_x\text{PbI}_3$ composition. Allowing to cool to room temperature after annealed, spiro-OMeTAD was covered with the PVK layer by mult-step spin-coated (700 rpm for 5 s and 3500 rpm for 20 s) to form a hole transport layer, which was prepared by dissolved 75 mg spiro-OMeTAD in 1mL chlorobenzene, then added 28.8 μL tBP and 17.5 μL Li-TFSI solution (520 mg Li-TFSI dissolved in 1 mL acetonitrile). A 100 nm thickness of silver electrode was deposited on HTL by thermal evaporation. Finally, a planar perovskite with active area of $0.3 \times 0.3 \text{ cm}^2$ thus was obtained.

4.3. Characterization

Surface morphologies of ETL films, PbI_2 films, perovskite films, and cross-view structure of KFBS-modified PSCs were observed by FE-SEM (JSM-7610F Plus, Japan). The grain sizes of the perovskite were calculated by the software: Nano Measurer 1.2. XPS and UPS were executed by Thermo Fisher Scientific K-Alpha+. The roughness of the PVK films and ETL films were measured by AFM (Multimode-8J). AFM measurements were conducted using an

intelligent mode with a scan rate of 0.977 Hz. The crystal structures of the PVK films were characterized through XRD (Smart Lab 3 KW, Japan). FTIR spectrum was obtained from Nicolet iZ10 spectrometer (Thermo Scientific, USA).

The photoluminescence emission spectra (PL) were measured by a fluorescence spectrophotometer (LF-1303003, Thermo Scientific Lumina, America) with an excitation wavelength of 534 nm. The time-resolved PL decay (TRPL) was performed by an Omin- λ Monochromator/Spectrograph (Zolix) using an excitation wavelength of 800 nm. The UV-vis absorption spectra and the optical transmission spectra were measured by UV-vis spectrometer (PerkinElmer Lambda 1050). The Zeta potential was characterized by NanoBrook Omni. IPCE was analyzed by an EQE measurement system (Enli technology Co., Ltd). Capacitance-voltage, electrical impedance spectroscopy (EIS), Mott-Schottky (M-S) curves and transient photovoltage (TPV) measurements were taken at an electrochemical workstation (IM6ex, Zahner, Germany) under ambient condition ($30\% \pm 5\%$ relative humidity). The current density vs voltage curve (J - V) was measured using a Keithley 2420 source-measurement source simulating sunlight (AM 1.5G) based on an illumination intensity of 100 mW cm^{-2} and the light intensity was standardizing with NREL-calibrated silicon solar cells (KG-2 filter), which was measured under ambient conditions ($30\% \pm 5\%$ relative humidity). At the same time, through the J - V measurement of multiple devices, the corresponding statistical diagram was made to record the repeatability of PSCs.

Declaration of Competing Interest

The authors declare that they have no known competing financial interests or personal relationships that could have appeared to influence the work reported in this paper.

Acknowledgments

The authors acknowledge the joint support from the National Natural Science Foundation of China (No. 51972123, U1705256 and 21771066). Thanks for the testing service provided by the IACHQU.

Appendix A. Supplementary Materials

Supplementary Materials to this article can be found online at <https://doi.org/10.1016/j.cej.2022.xxxxxx>.

References

- [1] G. Kim, H. Min, K. Lee, D. Lee, S. Yoon, S. Seok, Impact of strain relaxation on performance of alpha-formamidinium lead iodide perovskite solar cells, *Science* 370 (2020) 108-112.
- [2] C. Zuo, H. Bolink, H. Han, J. Huang, D. Cahen, L. Ding, Advances in Perovskite Solar Cells, *Adv. Sci.* 3 (2016) 1500324.
- [3] L. Ono, N. Park, K. Zhu, W. Huang, Y. Qi, Perovskite Solar Cells—Towards Commercialization, *ACS Energy Letters* 2(8) (2017) 1749-1751.
- [4] A. Kojima, K. Teshima, Y. Shirai, T. Miyasaka, Organometal Halide Perovskites as Visible-Light Sensitizers for Photovoltaic Cells, *J. Am. Chem. Society.* 131(17) (2009) 6050-6051.
- [5] Best research-cell efficiencies, National Renewable Energy Laboratory (NREL), <https://www.nrel.gov/pv/cell-efficiency.html> (accessed: 2022-01-26).
- [6] L. Lin, T. Jones, T. Yang, N. Duffy, J. Li, L. Zhao, B. Chi, X. Wang, G. Wilson, Inorganic Electron Transport Materials in Perovskite Solar Cells, *Advanced Functional Materials* 31(5) (2020).
- [7] W. Hu, S. Yang, S. Yang, Surface Modification of TiO₂ for Perovskite Solar Cells, *Trends in Chemistry* 2(2) (2020) 148-162.
- [8] Q. Guo, J. Wu, Y. Yang, X. Liu, W. Sun, Y. Wei, Z. Lan, J. Lin, M. Huang, H. Chen, Y. Huang, Low-temperature processed rare-earth doped brookite TiO₂ scaffold for UV stable, hysteresis-free and high-performance perovskite solar cells, *Nano Energy* 77 (2020) 105183.
- [9] N. Li, R. Guo, W. Chen, V. Körstgens, J. Heger, S. Liang, C. Brett, M. Hossain, J. Zheng, P. Deimel, A. Buyruk, F. Allegretti, M. Schwartzkopf, J. Veinot, G. Schmitz, J. Barth, T. Ameri, S. Roth, P.

- Müller-Buschbaum, Tailoring Ordered Mesoporous Titania Films via Introducing Germanium Nanocrystals for Enhanced Electron Transfer Photoanodes for Photovoltaic Applications, *Advanced Functional Materials* 31 (2021) 2102105.
- [10] Y. Zhang, X. Liu, P. Li, Y. Duan, X. Hu, F. Li, Y. Song, Dopamine-crosslinked TiO₂/perovskite layer for efficient and photostable perovskite solar cells under full spectral continuous illumination, *Nano Energy* 56 (2019) 733-740.
- [11] J. Christians, P. Schulz, J. Tinkham, T. Schloemer, S. Harvey, B.J. Tremolet de Villers, A. Sellinger, J.J. Berry, J.M. Luther, Tailored interfaces of unencapsulated perovskite solar cells for >1,000 hour operational stability, *Nature Energy* 3(1) (2018) 68-74.
- [12] Q. Jiang, X. Zhang, J. You, SnO₂ : A Wonderful Electron Transport Layer for Perovskite Solar Cells, *Small* (2018) e1801154.
- [13] Y. Tu, J. Wu, G. Xu, X. Yang, R. Cai, Q. Gong, R. Zhu, W. Huang, Perovskite Solar Cells for Space Applications: Progress and Challenges, *Adv Mater* 33(21) (2021) e2006545.
- [14] C. Altinkaya, E. Aydin, E. Ugur, F. Isikgor, A. Subbiah, M. De Bastiani, J. Liu, A. Babayigit, T. Allen, F. Laquai, A. Yildiz, S. De Wolf, Tin Oxide Electron-Selective Layers for Efficient, Stable, and Scalable Perovskite Solar Cells, *Adv Mater* 33(15) (2021) e2005504..
- [15] L. Xiong, Y. Guo, J. Wen, H. Liu, G. Yang, P. Qin, G. Fang, Review on the Application of SnO₂ in Perovskite Solar Cells, *Advanced Functional Materials* 28(35) (2018) 1802757.
- [16] Q. Jiang, L. Zhang, H. Wang, X. Yang, J. Meng, H. Liu, Z. Yin, J. Wu, X. Zhang, J. You, Enhanced electron extraction using SnO₂ for high-efficiency planar-structure HC(NH₂)₂PbI₃-based perovskite solar cells, *Nature Energy* 2(1) (2017) 16177.
- [17] H. Min, D. Lee, J. Kim, G. Kim, K. Lee, J. Kim, M. Paik, Y. Kim, K. Kim, M. Kim, T. Shin, S. Il Seok, Perovskite solar cells with atomically coherent interlayers on SnO₂ electrodes, *Nature* 598 (2021) 444-450.
- [18] S. Huang, P. Li, J. Wang, J. Huang, Q. Xue, N. Fu, Modification of SnO₂ electron transport Layer: Brilliant strategies to make perovskite solar cells stronger, *Chem. Eng. J.* 439 (2022) 135687.
- [19] C. Wang, J. Wu, S. Wang, X. Liu, X. Wang, Z. Yan, L. Chen, X. Liu, G. Li, W. Sun, Z. Lan, Alkali Metal Fluoride-Modified Tin Oxide for n-i-p Planar Perovskite Solar Cells, *ACS Appl Mater Interfaces* 13(42) (2021) 50083-50092.

- [20] R. Yuan, B. Cai, Y. Lv, X. Gao, J. Gu, Z. Fan, X. Liu, C. Yang, M. Liu, W. Zhang, Boosted charge extraction of NbOx-enveloped SnO₂ nanocrystals enables 24% efficient planar perovskite solar cells, *Energy & Environmental Science* 14(9) (2021) 5074-5083.
- [21] S. Park, K. Zhu, Advances in SnO₂ for Efficient and Stable n-i-p Perovskite Solar Cells, *Adv Mater* (2022) e2110438.
- [22] J. Zhang, J. Fu, Q. Chen, H. Ma, Z. Jiang, Z. Zhang, Y. Zhou, B. Song, 3,5-Difluorophenylboronic acid-modified SnO₂ as ETLs for perovskite solar cells: PCE > 22.3%, T82 > 3000 h, *Chemical Engineering Journal* 433 (2022) 133744.
- [23] P. Wang, B. Chen, R. Li, S. Wang, N. Ren, Y. Li, S. Mazumdar, B. Shi, Y. Zhao, X. Zhang, Cobalt Chloride Hexahydrate Assisted in Reducing Energy Loss in Perovskite Solar Cells with Record Open-Circuit Voltage of 1.20 V, *ACS Energy Letters* 6 (2021) 2121-2128.
- [24] X. Guo, X. Huang, J. Su, Z. Lin, J. Ma, J. Chang, Y. Hao, Reducing the interfacial energy loss via oxide/perovskite heterojunction engineering for high efficient and stable perovskite solar cells, *Chemical Engineering Journal* 417 (2021) 129184.
- [25] Z. Xing, S. Lin, X. Meng, T. Hu, D. Li, B. Fan, Y. Cui, F. Li, X. Hu, Y. Chen, A Highly Tolerant Printing for Scalable and Flexible Perovskite Solar Cells, *Advanced Functional Materials* 31(50) (2021) 2107726.
- [26] Y. Dong, W. Shen, W. Dong, C. Bai, J. Zhao, Y. Zhou, F. Huang, Y.B. Cheng, J. Zhong, Chlorobenzenesulfonic Potassium Salts as the Efficient Multifunctional Passivator for the Buried Interface in Regular Perovskite Solar Cells, *Advanced Energy Materials* 12 (2022) 2200417.
- [27] J. Zhang, X. Xing, D. Qian, A. Wang, L. Gu, Z. Kuang, J. Wang, H. Zhang, K. Wen, W. Xu, M. Niu, X. Du, L. Yuan, C. Cao, Y. Cao, L. Zhu, N. Wang, C. Yi, W. Huang, J. Wang, Sulfonic Zwitterion for Passivating Deep and Shallow Level Defects in Perovskite Light-Emitting Diodes, *Advanced Functional Materials* 32 (2022) 2111578.
- [28] P. Zhu, S. Gu, X. Luo, Y. Gao, S. Li, J. Zhu, H. Tan, Simultaneous Contact and Grain-Boundary Passivation in Planar Perovskite Solar Cells Using SnO₂-KCl Composite Electron Transport Layer, *Advanced Energy Materials* 10(3) (2020) 1903083.
- [29] E. Jung, B. Chen, K. Bertens, M. Vafaie, S. Teale, A. Proppe, Y. Hou, T. Zhu, C. Zheng, E.H. Sargent, Bifunctional Surface Engineering on SnO₂ Reduces Energy Loss in Perovskite Solar Cells, *ACS*

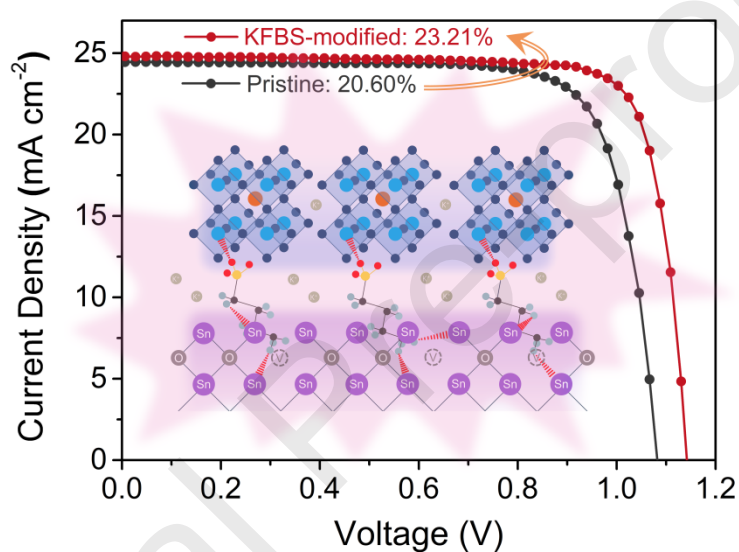
- Energy Letters 5(9) (2020) 2796-2801.
- [30] K. Choi, J. Lee, H. Kim, C. Park, G. Kim, H. Choi, S. Park, S. Park, T. Park, Thermally stable, planar hybrid perovskite solar cells with high efficiency, *Energy & Environ. Sci.* 11 (2018) 3238-3247..
- [31] D. Wang, H. Liu, M. Li, D. Xia, J. Holoubek, Z. Deng, M. Yu, J. Tian, Z. Shan, S.P. Ong, P. Liu, Z. Chen, A long-lasting dual-function electrolyte additive for stable lithium metal batteries, *Nano Energy* 75 (2020) 104889.
- [32] V. Hoang, S. Lee, C.W. Bark, Dispersed SnO₂ colloids using sodium dodecyl benzene sulfonate for high-performance planar perovskite solar cells, *Solar Energy* 230 (2021) 747-753.
- [33] M. Khademi, W. Wang, W. Reitering, D. Barz, Zeta Potential of Poly(methyl methacrylate) (PMMA) in Contact with Aqueous Electrolyte–Surfactant Solutions, *Langmuir* 33 (2017) 10473-10482.
- [34] Q. Guo, J. Wu, Y. Yang, X. Liu, Z. Lan, J. Lin, M. Huang, Y. Wei, J. Dong, J. Jia, Y. Huang, High-Performance and Hysteresis-Free Perovskite Solar Cells Based on Rare-Earth-Doped SnO₂ Mesoporous Scaffold, *Research* 2019 (2019) 4049793.
- [35] J. Chen, X. Zhao, S. Kim, N. Park, Multifunctional Chemical Linker Imidazoleacetic Acid Hydrochloride for 21% Efficient and Stable Planar Perovskite Solar Cells, *Adv Mater* 31 (2019) e1902902.
- [36] J. Hong, E.D. Jung, J. Yu, D. Kim, Y. Nam, I. Oh, E. Lee, J. Yoo, S. Cho, M. Song, Improved Efficiency of Perovskite Solar Cells Using a Nitrogen-Doped Graphene-Oxide-Treated Tin Oxide Layer, *ACS Appl Mater Interfaces* 12(2) (2020) 2417-2423.
- [37] Y. Han, H. Xie, E. Lim, D. Bi, Review of Two-Step Method for Lead Halide Perovskite Solar Cells, *Solar RRL* 6 (2022) 2101007.
- [38] M. Saliba, T. Matsui, K. Domanski, J. Seo, A. Ummadisingu, S. Zakeeruddin, J. Correa-Baena, W. Tress, A. Abate, A. Hagfeldt, M. Grätzel, Incorporation of rubidium cations into perovskite solar cells improves photovoltaic performance, *Science* 354 (2016) 206-209.
- [39] T. Bu, X. Liu, Y. Zhou, J. Yi, X. Huang, L. Luo, J. Xiao, Z. Ku, Y. Peng, F. Huang, Y. Cheng, J. Zhong, A novel quadruple-cation absorber for universal hysteresis elimination for high efficiency and stable perovskite solar cells, *Energy & Environmental Science* 10 (2017) 2509-2515.
- [40] C. Zhang, Y. Wang, X. Lin, T. Wu, Q. Han, Y. Zhang, L. Han, Effects of A site doping on the crystallization of perovskite films, *Journal of Materials Chemistry A* 9(3) (2021) 1372-1394.

- [41] T. Jacobsson, J. Correa-Baena, E. Halvani Anaraki, B. Philippe, S. Stranks, M. Bouduban, W. Tress, K. Schenk, J. Teuscher, J. Moser, H. Rensmo, A. Hagfeldt, Unreacted PbI_2 as a Double-Edged Sword for Enhancing the Performance of Perovskite Solar Cells, *J. Am. Chem. Soc.* 138 (2016) 10331-10343.
- [42] Y. Kim, N. Jeon, J. Noh, W. Yang, J. Seo, J. Yun, A. Ho-Baillie, S. Huang, M. Green, J. Seidel, T. Ahn, S. Seok, Beneficial Effects of PbI_2 Incorporated in Organo-Lead Halide Perovskite Solar Cells, *Advanced Energy Materials* 6 (2016) 1502104.
- [43] A. Merdasa, A. Kiligaris, C. Rehmann, M. Abdi-Jalebi, J. Stöber, B. Louis, M. Gerhard, S. Stranks, E. Unger, I. Scheblykin, Impact of Excess Lead Iodide on the Recombination Kinetics in Metal Halide Perovskites, *ACS Energy Letters* 4 (2019) 1370-1378.
- [44] S. You, H. Zeng, Z. Ku, X. Wang, Z. Wang, Y. Rong, Y. Zhao, X. Zheng, L. Luo, L. Li, S. Zhang, M. Li, X. Gao, X. Li, Multifunctional Polymer-Regulated SnO_2 Nanocrystals Enhance Interface Contact for Efficient and Stable Planar Perovskite Solar Cells, *Advanced Materials* 32 (2020) 2003990.
- [45] H. Ma, M. Wang, Y. Wang, Q. Dong, J. Liu, Y. Yin, J. Zhang, M. Pei, L. Zhang, W. Cai, L. Shi, W. Tian, S. Jin, J. Bian, Y. Shi, Asymmetric organic diammonium salt buried in SnO_2 layer enables fast carrier transfer and interfacial defects passivation for efficient perovskite solar cells, *Chem. Eng. J.* 442 (2022) 136291..
- [46] T. Singh, S. Oz, A. Sasinska, R. Frohnhoven, S. Mathur, T. Miyasaka, Sulfate-Assisted Interfacial Engineering for High Yield and Efficiency of Triple Cation Perovskite Solar Cells with Alkali-Doped TiO_2 Electron-Transporting Layers, *Advanced Functional Materials* 28(14) (2018) 1706287.
- [47] J. Zhu, Y. Qian, Z. Li, O. Gong, Z. An, Q. Liu, J. Choi, H. Guo, P. Yoo, D. Kim, T. Ahn, G. Han, H. Jung, Defect Healing in $\text{FAPb}(\text{I}_{1-x}\text{Br}_x)_3$ Perovskites: Multifunctional Fluorinated Sulfonate Surfactant Anchoring Enables >21% Modules with Improved Operation Stability, *Advanced Energy Materials* 12 (2022) 2200632.
- [48] X. Liu, J. Wu, Y. Yang, D. Wang, G. Li, X. Wang, W. Sun, Y. Wei, Y. Huang, M. Huang, L. Fan, Z. Lan, J. Lin, K. Ho, Additive Engineering by Bifunctional Guanidine Sulfamate for Highly Efficient and Stable Perovskites Solar Cells, *Small* 16 (2020) e2004877.
- [49] Y. Raoui, H. Ez-Zahraoui, S. Kazim, S. Ahmad, Energy level engineering of charge selective contact and halide perovskite by modulating band offset: Mechanistic insights, *Journal of Energy Chemistry*

- 54 (2021) 822-829.
- [50] G. Li, J. Song, J. Wu, Z. Song, X. Wang, W. Sun, L. Fan, J. Lin, M. Huang, Z. Lan, P. Gao, Efficient and Stable 2D@3D/2D Perovskite Solar Cells Based on Dual Optimization of Grain Boundary and Interface, *ACS Energy Letters* 6 (2021) 3614-3623.
- [51] J. Duan, Y. Zhao, X. Yang, Y. Wang, B. He, Q. Tang, Lanthanide Ions Doped CsPbBr₃ Halides for HTM-Free 10.14%-Efficiency Inorganic Perovskite Solar Cell with an Ultrahigh Open-Circuit Voltage of 1.594 V, *Advanced Energy Materials* 8(31) (2018) 1802346.
- [52] W. Wu, P.N. Rudd, Z. Ni, C.H. Van Brackle, H. Wei, Q. Wang, B.R. Ecker, Y. Gao, J. Huang, Reducing Surface Halide Deficiency for Efficient and Stable Iodide-Based Perovskite Solar Cells, *Journal of the American Chemical Society* 142(8) (2020) 3989-3996.
- [53] J. Tao, X. Liu, J. Shen, H. Wang, J. Xue, C. Su, H. Guo, G. Fu, W. Kong, S. Yang, Functionalized SnO₂ films by using EDTA-2 M for high efficiency perovskite solar cells with efficiency over 23%, *Chemical Engineering Journal* 430 (2022) 132683.
- [54] Q. Zhou, J. Duan, X. Yang, Y. Duan, Q. Tang, Interfacial Strain Release from the WS₂/CsPbBr₃ van der Waals Heterostructure for 1.7 V Voltage All-Inorganic Perovskite Solar Cells, *Angew Chem Int Ed* 59 (2020) 21997-22001.
- [55] W. Hui, Y. Yang, Q. Xu, H. Gu, S. Feng, Z. Su, M. Zhang, J. Wang, X. Li, J. Fang, F. Xia, Y. Xia, Y. Chen, X. Gao, W. Huang, Red-Carbon-Quantum-Dot-Doped SnO₂ Composite with Enhanced Electron Mobility for Efficient and Stable Perovskite Solar Cells, *Adv. Mater.* 32 (2020) 1906374.
- [56] D. Yang, R. Yang, X. Ren, X. Zhu, Z. Yang, C. Li, S.F. Liu, Hysteresis-Suppressed High-Efficiency Flexible Perovskite Solar Cells Using Solid-State Ionic-Liquids for Effective Electron Transport, *Adv Mater* 28(26) (2016) 5206-5213.
- [57] W. Hu, W. Zhou, X. Lei, P. Zhou, M. Zhang, T. Chen, H. Zeng, J. Zhu, S. Dai, S. Yang, S. Yang, Low-Temperature In Situ Amino Functionalization of TiO₂ Nanoparticles Sharpens Electron Management Achieving over 21% Efficient Planar Perovskite Solar Cells, *Adv Mater* 31 (2019) e1806095..
- [58] M. Li, X. Yan, Z. Kang, Y. Huan, Y. Li, R. Zhang, Y. Zhang, Hydrophobic Polystyrene Passivation Layer for Simultaneously Improved Efficiency and Stability in Perovskite Solar Cells, *ACS Applied Materials & Interfaces* 10 (2018) 18787-18795.

- [59] S. Yu, Y. Yan, Y. Chen, P. Chábera, K. Zheng, Z. Liang, Enabling room-temperature processed highly efficient and stable 2D Ruddlesden-Popper perovskite solar cells with eliminated hysteresis by synergistic exploitation of additives and solvents, *J. Mater. Chem. A* 7 (2019) 2015-2021.

TOC



Declaration of Competing Interests

The authors declare that they have no known competing financial interests or personal relationships that could have appeared to influence the work reported in this paper.

Highlights

- Multifunctional Potassium nonafluoro-1-buthanesulfonate (KFBS) is implanted into ETL;
- Synergistic effect of K ion, sulfonic and nonafluorobutane group in KFBS is verified;
- Energy match between PVK and ETL is tuned, and various defects are passivated;
- Efficiency increases from 20.6% for pristine one to 23.2% for KFBS-modified device.